SMC-TR-00-38

AEROSPACE REPORT NO.
TR-96(1550)-1

Raman Lidar Calibration for the DMSP SSM/T-2 Microwave Water Vapor Sensor

August 2000

Prepared by

J. E. WESSEL
Laboratory Operations
Engineering and Technology Group

S. M. BECK, Y. C. CHAN, R. W. FARLEY, and J. A. GELBWACHS
Ground Systems Development & Operations Department
Engineering and Technology Group

Prepared for

SPACE AND MISSILE SYSTEMS CENTER
AIR FORCE MATERIEL COMMAND
2430 E. El Segundo Boulevard
Los Angeles Air Force Base, CA 90245

Contract No. F04701-93-C-0094

Space Systems Group

THE AEROSPACE CORPORATION
El Segundo, California

This report was submitted by The Aerospace Corporation, El Segundo, CA 90245-4691, under Contract No. F04701-93-C-0094 with the Space and Missile Systems Center, P. O. Box 92960, Los Angeles, CA 90009-2960. It was reviewed and approved for The Aerospace Corporation by D. J. Gorney, Associate Principal Director. The project officer is Mr. John Tomaszewski.

This report has been reviewed by the Public Affairs Office (PAS) and is releasable to the National Technical Information Service (NTIS). At NTIS, it will be available to the general public, including foreign nationals.

This technical report has been reviewed and is approved for publication. Publication of this report does not constitute Air Force approval of the report's findings or conclusions. It is published only for the exchange and stimulation of ideas.

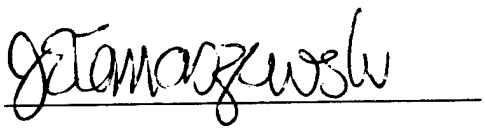

Mr. John Tomaszewski
Project Officer

REPORT DOCUMENTATION PAGE

Form Approved
OMB No. 0704-0188

1. AGENCY USE ONLY (Leave blank)	2. REPORT DATE	3. REPORT TYPE AND DATES COVERED
	August 2000	

4. TITLE AND SUBTITLE

Raman Lidar Calibration for the DMSP SSM/T-2 Microwave Water Vapor Sensor

5. FUNDING NUMBERS

F04701-93-C-0094

6. AUTHOR(S)

J. E. Wessel, S. M. Beck, Y. C. Chan, R. W. Farley, and J. A. Gelbwachs

7. PERFORMING ORGANIZATION NAME(S) AND ADDRESS(ES)

The Aerospace Corporation
2350 El Segundo Boulevard
El Segundo, CA 90245

8. PERFORMING ORGANIZATION REPORT NUMBER

TR-96(1550)-1

9. SPONSORING/MONITORING AGENCY NAME(S) AND ADDRESS(ES)

Space and Missile Systems Center
Air Force Materiel Command
2430 E. El Segundo Boulevard
Los Angeles Air Force Base, CA 90245

10. SPONSORING/MONITORING AGENCY REPORT NUMBER

SMC-TR-00-38

11. SUPPLEMENTARY NOTES

12a. DISTRIBUTION/AVAILABILITY STATEMENT

Approved for public release; distribution unlimited.

12b. DISTRIBUTION CODE

13. ABSTRACT (Maximum 200 words)

Campaigns were conducted at the Pacific Missile Range Facility, Barking Sands, Kauai, investigating Raman lidar as a method to improve calibration of the DMSP SSM/T-2 microwave water vapor profiling instrument. Lidar mixing ratios were calibrated against AIR and Vaisala radiosondes and the calibration was tested in the vicinity of clouds. Above 6 km, radiosondes reported anomalously low relative humidity in the vicinity of clouds. Lidar measurements were confirmed by using an electro-optical shutter, which provided correct measurement of relative humidity at cloud bases above 6 km. Radiative transfer calculations applied to the lidar data closely matched signals observed in the SSM/T-2 atmospheric channels. Forward calculations for surface sensitive channels disagreed with SSM/T-2 and SSM/I observations. Fine scale surface roughness and localized orographic drying are tentatively suggested as explanations. Cloud effects were ruled out as a significant source of discrepancy.

14. SUBJECT TERMS

Atmospheric measurements, calibration, humidity, laser radar, remote sensing, satellite.

15. NUMBER OF PAGES

15

16. PRICE CODE

17. SECURITY CLASSIFICATION OF REPORT	18. SECURITY CLASSIFICATION OF THIS PAGE	19. SECURITY CLASSIFICATION OF ABSTRACT	20. LIMITATION OF ABSTRACT
Unclassified	Unclassified	Unclassified	

Contents

Figures

Tables

Abstract—**Campaigns were conducted at the Pacific Missile Range Facility, Barking Sands, Kauai, investigating Raman lidar as a method to improve calibration of the DMSP SSM/T-2 microwave water vapor profiling instrument. Lidar mixing ratios were calibrated against AIR and Vaisala radiosondes and the calibration was tested in the vicinity of clouds. Above 6 km, radiosondes reported anomalously low relative humidity in the vicinity of clouds. Lidar measurements were confirmed by using an electro-optical shutter, which provided correct measurement of relative humidity at cloud bases above 6 km. Radiative transfer calculations applied to the lidar data closely matched signals observed in the SSM/T-2 atmospheric channels. Forward calculations for surface sensitive channels disagreed with SSM/T- 2 and SSM/I observations. Fine scale surface roughness and localized orographic drying are tentatively suggested as explanations. Cloud effects were ruled out as a significant source of discrepancy.**

Index Terms—**Atmospheric measurements, calibration, humidity, laser radar, remote sensing, satellite.**

I. Introduction

CONVENTIONAL calibration of the DMSP SSM/T-2 microwave water vapor profiler [1]–[3] relies on comparison between radiosonde ground truth and satellite measurements, or between satellite measurements and underflights by an ER-2 equipped with a similar microwave radiometer [2], [3]. Intercomparison errors are substantial for these approaches. In this paper, we report on a two-part campaign designed to improve ground truth for satellite calibration. Measurements from a Raman water vapor lidar were compared to radiosonde data and indirectly, to satellite microwave measurements. In the second part, the lidar was improved and used to obtain definitive calibration data.

Radiosonde humidity sensors are subject to bias at low temperatures [4], [5] and sampling errors contribute uncertainty due to time and spatial variability of water vapor. Several recent studies compared radiosonde relative humidity (RH) profiles with those derived from lidar [4], [6], upward microwave radiometry [7], and downward aircraft microwave radiometry [8], and frost point hygrometers [9]. Systematic tendencies were identified in which Vaisala radiosonde RH values were low relative to lidar above about 8 km [5], [6] and AIR radiosondes with carbon hygristors reported high for midtroposphere altitudes in low humidity regimes. Lidar measurements were limited to altitudes below about 9 km due to declining water vapor signal levels. Photomultiplier nonlinearity (after-pulsing [10]) was also cited as a factor reducing reliability of lidar measurements above this altitude. The biases and limitations have an important impact on satellite radiometer calibration. It would be desirable to build a statistical data base of collocated satellite microwave brightness temperatures calibrated to ±1 K or better, with corresponding atmospheric profiles extending from 0 to 12 km, for a range of representative atmospheric conditions. This is a challenge for existing technology, particularly for the upper troposphere channels of satellite microwave radiometers. The work reported in this paper addresses improvements in Raman lidar measurement that have the potential to improve calibration range and accuracy. Observation conditions were significantly different than in prior work, system parameters were somewhat different, and the primary radiosondes used different water vapor sensors than those employed in prior lidar studies.

A transportable Raman lidar developed at the Aerospace Corporation was deployed to an island test site at Pacific Missile Range Facility, Barking Sands, Kauai (PMRFK) following launch of DMSP F-14. The site was selected for a tropical atmosphere, minimal cloud cover, and small land area relative to the T-2 footprint. Water has a low surface emissivity that can be estimated by calculation. The low surface emissivity improves the contrast between signals arising from the lower troposphere and from the surface. The lidar operated in conjunction with AIR and Vaisala radiosondes and was supported by downlinked satellite data and surface measurements from a regional buoy network. Raman lidar profiles extending from < 0.5 to > 10 km altitude were obtained on 34 of 37 available nights.

II. Experimental

The lidar transmitted 355 nm output from a frequency-tripled Nd : YAG laser (Spectra Physics GCR290-50, injection locked), and received backscattered returns with a f/6.5 0.8 m diameter (primary) Cassegrain telescope employed in coaxial configuration, as shown in Fig. 1. Laser, telescope, detection optics, and electronics were installed in a 30 ft long container that was transported by air to PMRFK. The telescope field of view was selected to be 1 mr. Typical laser output of 15 W at 355 nm and 50 Hz was expanded to 10 cm diameter and injected by a diagonal mirror into the excluded central region of the Cassegrain telescope. Beam/telescope colinearity was achieved using a corner cube retroreflector. The 355 nm beam expander/collimator was adjusted for parallel wavefront output (<10 μr divergence) by monitoring interference fringes in a flat etalon plate. The lidar return beam was separated into three channels (elastic Rayleigh–Mie channel at 355 nm, a nitrogen

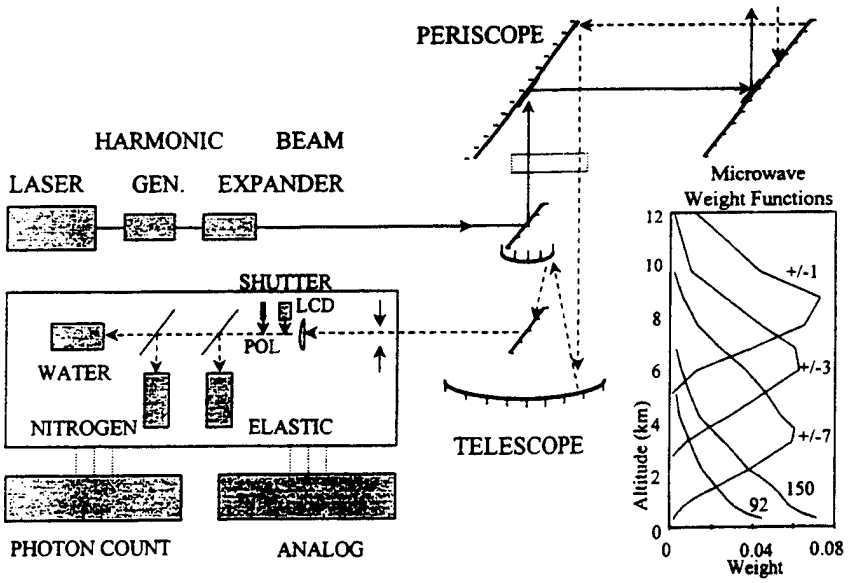

Fig. 1. Schematic diagram of the Aerospace Raman lidar. The closed rectangle represents the light-tight housing for photomultipliers, beam splitters and filter sets. Electrical output signals are split between photon-counting and analog detection systems. The removable ferroelectric liquid crystal and polarizer are not shown. Microwave weighting functions characterizing the SSM/T-2 water vapor sensor response are shown in the insert (lower right-hand area) for the climatology of 20 N, 160 W, June.

Raman channel at 386 nm, and a water vapor Raman channel at 407 nm) by dichroic mirrors and isolated by narrow band interference filters. For the June–July campaign, filter (CVI) bandwidths were 2 nm with peak transmissions of 35%. In September, a new set of filters (Barr) was employed with bandwidths of 4 nm and transmissions of 70%. Spectral selectivity was verified by inserting sharp cut-off filters into the return beam. It was possible to fully attenuate the Rayleigh–Mie signal while preserving nitrogen and water Raman signals by using a UV cut-off filter (Schott GG385, 3 mm). The nitrogen Raman signal was attenuated while retaining water Raman by using a red shifted cut-off filter (Schott GG400, 3 mm). The water signal persisted in the presence of an additional UV transmitting visible cut-off filter (Corning 7-54). Therefore the narrowband interference filters effectively isolated the desired Raman signals. This was confirmed by the absence of spurious signals in the water channel in the presence of low clouds, using the CVI filter set. The Barr filter set provided less out-of-band rejection, resulting in occasional small increase of water channel signal for range bins corresponding to high altitude clouds.

Photomultiplier detectors (EMI 9235QA) operated in photon-counting mode for altitudes above 2 km and analog mode below 2 km. Signals were collected with varying attenuation in order to minimize photomultiplier and photon-counting nonlinearities [11]. The lidar was equipped with a beam director periscope that scanned over a hemisphere. It was used to test the validity of low altitude measurements and to measure horizontal variability. However, periscope transmission losses reduced signals, therefore it was not used routinely. Photon-counting equipment was set up with 80 ns range bins, corresponding to 12 m altitude increments. For purposes of analysis and presentation, data was averaged over multiple bins, with increasing time intervals for increasing ranges, thereby improving the signal-to-noise ratio at higher altitudes. Bin widths corresponded to 24 m increments in the 0–3 km range, 48 m for 3–5 km, 96 m for 5–6 km, 192 m for 6–9 km, and 0.3 km beyond 9 km range. The standard data acquisition interval was 15 000 pulses, corresponding to 5 min collection time. The water channel photon-counting signal-to-noise ratio declined from about 50 at 4 km range to 25 at 10 km range under these conditions. On occasion, standard parameters were changed in order to study transient phenomenon, to seek cloud-free observation windows, or for high altitude measurements. In the second campaign, a high-speed ferroelectric liquid crystal shutter was added to the optical train in order to suppress spurious signal-induced noise in high altitude measurements. When a voltage pulse was applied, the 407 nm signal polarization rotated such that it was transmitted through the optical train. (Returning 407 nm was primarily linearly polarized because the transmitted laser beam is linearly polarized and water vapor Raman scattering is only weakly depolarized by molecular asymmetry [12].) This system provided a 10:1 on/off ratio, blocking 90% of the water signal during the first 10 μs. Blocking was less for the nitrogen and Rayleigh channels. Fortunately, saturation is of less concern for these because the Rayleigh is not used quantitatively and the nitrogen signal has much less dynamic range than the water channel. A ferroelectric liquid crystal was chosen because it switches at higher speed than conventional liquid crystal media, while retaining the large acceptance angle and aperture of these devices. The Raman signals are near the uv cut-off edge of the ferroelectric material, therefore the shutter is only practical for wavelengths longer than 350 nm.

Results discussed below obtained with the optical shutter confirmed that photomultiplier after-pulse effects distorted high altitude water vapor signals. Although it was previously suggested that correction for the effect is unreliable [6], a simple waveform subtraction procedure provided moderately successful correction. The success may be due to the relatively stable after-

pulse waveform produced by the EMI 9235 photomultiplier, or it may be due to the high atmospheric transmission experienced in Kauai, resulting in larger high altitude signals. The lidar calibration constant, C_1 in (1) below, relates the ratio between water and nitrogen signals to the water vapor mixing ratio (MR)

$$\begin{aligned} \mathrm{MR}(h) = C_1 \cdot [\mathrm{T(N_2)/T(H_2O)}] \\ [\mathrm{S(H_2O)} - \mathrm{DC(H_2O)} - C_2 \cdot \mathrm{AP(H_2O)}] \\ /[\mathrm{S(N_2)} - \mathrm{DC(N_2)} - C_3 \cdot \mathrm{AP(N_2)}] \end{aligned} \quad (1)$$

where

(h)	altitude;
$\mathrm{T(N_2)}$	one-way transmission at the nitrogen Raman wavelength;
$\mathrm{T(H_2O)}$	transmission at the water Raman wavelength;
$\mathrm{S(H_2O)}$	water vapor Raman signal;
DC	dark current plus sky background (constant for all altitudes) determined from the vanishing signal at very large range;
AP	after-pulse signal;
C_2 and C_3	scaling factors for spurious after-pulse (AP) signals, which are described below.

[$\mathrm{AP(N_2)}$ and $\mathrm{DC(N_2)}$ are negligible and changes in $\mathrm{T(N_2)/T(H_2O)}$ due to differences in Rayleigh scattering were insignificant (<6%) across the range of interest.] RH is obtained from the mixing ratios

$$\mathrm{RH}(h) = 100 \cdot \mathrm{MR}(h)/\mathrm{MR}(h, \text{ saturation}) \quad (2)$$

where MR(saturation) is the saturated mixing ratio relative to liquid water determined from the radiosonde temperature profile. Saturation vapor pressure was estimated by an expression given by Liebe and Layton [14]

$$\begin{aligned} E_s = 0.610\,78 \cdot (\exp(((18.61 - T_c/240.7) \cdot T_c) \\ /(256.1 + T_c))) \quad \text{(kPa)} \end{aligned} \quad (3)$$

which closely models liquid water vapor pressures tabulated by the International Meteorological Organization (IMO), 1961 over the range 243–303K. Relative humidity profiles in the figures are referenced to liquid water for all temperatures. However, below 273K, grids have been added (thin dotted lines) indicating humidity relative to ice saturation vapor pressure. It is approximated by

$$\begin{aligned} E_s = 0.610\,78 \cdot (\exp(((23.63 - T_c/242.0223) \cdot T_c) \\ /(286.74 + T_c))) \quad \text{(kPa)} \end{aligned} \quad (4)$$

which approximates IMO tabulated values over the range 223–273K. Radiosonde measurements are referenced to liquid water vapor pressure at all temperatures because the sensor elements respond proportionally [13].

The lidar constant C_1 of (1) was derived from simultaneous radiosonde measurements. An AIR GPS 77 radiosonde system supplied temperature, relative humidity, and wind measurements. Polymeric film humidity sensors were used in the reported studies, in contrast to prior reported work [6], which employed AIR radiosondes equipped with carbon hygristors. Two lots of AIR radiosondes were used, one during June–July, some of which reported suspiciously low RH, unchanging over significant altitude ranges, sometimes including the surface level. The lot of new sondes, used in September, provided generally credible performance. Sondes were launched from the lidar site approximately 15 min prior to satellite overpass. Vaisala radiosondes (RS80) with polymeric humicap A sensors were launched simultaneously from an adjacent site at PMRFK on five nights of the September campaign. Vaisalas were also flown about 7 h after satellite overpass on eleven nights during June–July. Lidar data recorded in the presence of opaque clouds were used as validity checks for radiosonde measurements.

C_1 was determined daily and it reproduced to about ±2% as a result of system alignment using a large corner cube retroreflector. It was standard practice to derive calibration constants for the photon-counting mode from 3 to 6 km altitude data. This was based on the expectation of good photon-counting statistics, reasonable freedom from signal nonlinearity due to the appreciable range, moderately reliable operation of the radiosondes at temperatures prevailing in this range of altitudes, and relatively stable moisture content during observation periods. Viewing conditions were generally extremely clear, such that the nitrogen Raman signal levels were closely approximated by Rayleigh scattering losses for altitudes above 2 km.

In all cases, the calibration constants so derived yielded realistic saturation at cloud levels. The lidar calibration constant was derived by minimizing RMS difference between "good" AIR radiosondes from 3 to 6 km and the lidar mixing ratio profiles (~2% RH in typical cases). (Good radiosondes indicate the same relative change shown in the corresponding lidar measurement across changes in the water vapor profile for altitudes from 3 to 8 km. They also indicate 100% relative humidity in the presence of cloud liquid water.) C_1 did not change unless equipment parameters changed (e.g., filter sets or photomultiplier gain). Minimized RMS differences were larger for the Vaisala radiosondes and the changes in RH with altitude reported by the Vaisalas were physically inconsistent with changes in the water Raman channel. This is evident in Fig. 2, which compares profiles acquired simultaneously by AIR and Vaisala radiosondes. In Fig. 2(c) for example, the AIR sensor indicates RH rises from about 5% at 3 km to about 20% at 5 km, whereas the Vaisala shows a corresponding change from about 12–22%. The lidar signal increased by a factor 4 over this interval, agreeing with the AIR sonde. Similar behavior was observed between 3 and 4 km in Fig. 2(d) and between 5 and 8 km in Fig. 2(e). As discussed below, changes in lidar signal levels are highly reliable over this range of altitudes. This indicates that a systematic bias occurs in the Vaisala measurements at low RH, therefore AIR profiles were used for lidar calibration.

The lidar site was located at PMRF Barking Sands, approximately 300 m to the east of the north-south directed coastline. The altitude was approximately 5 m and surrounding terrain was generally level. A high bluff of the Kalalau coast was situated about 2 km north, extending eastward. Terrain to the east sloped upward toward Mt. Waialeale, altitude 1.5 km, at a distance of about 20 km. During June–July, prevailing surface winds were from the direction of Mt. Waialeale and afternoon

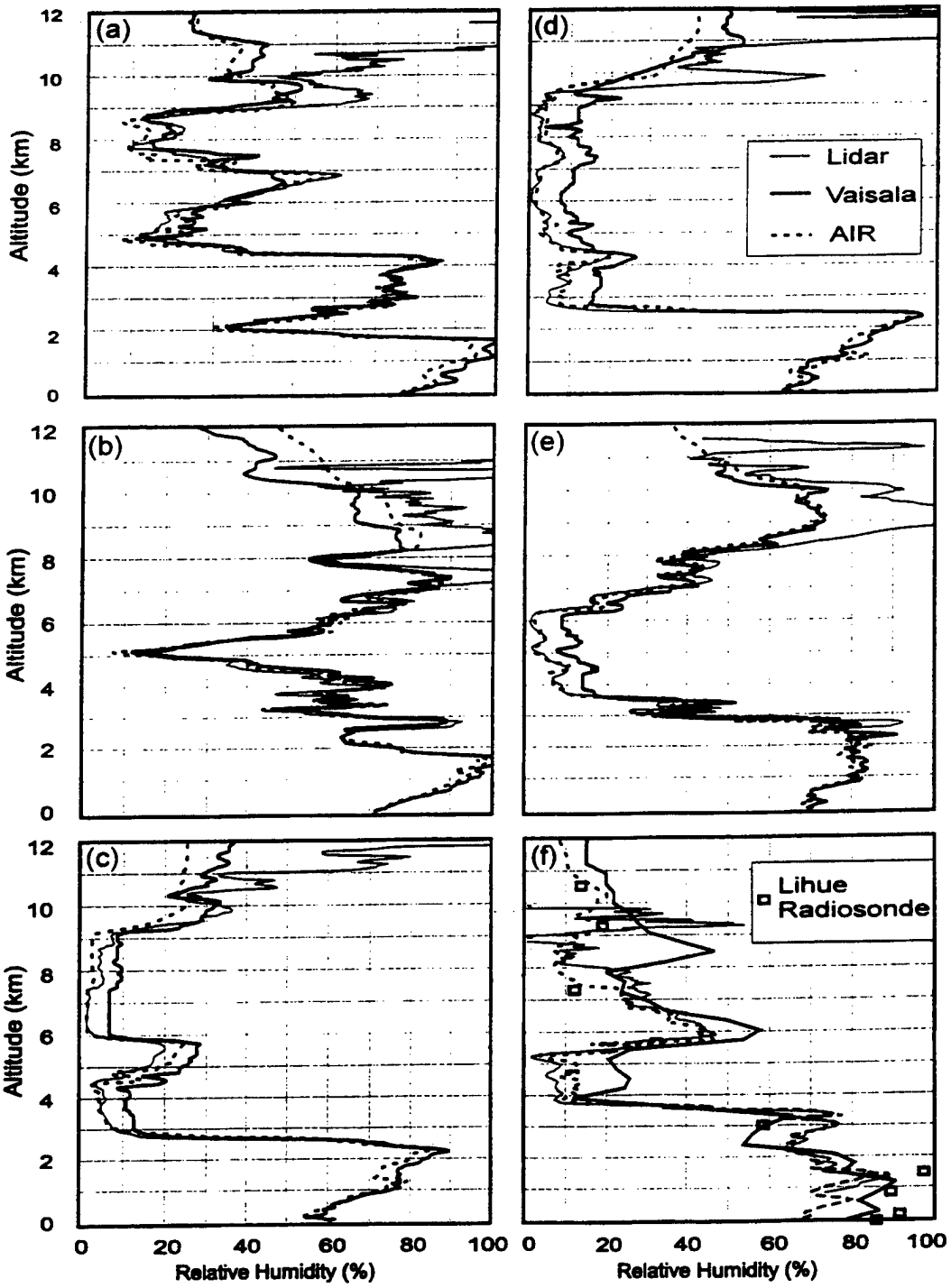

Fig. 2. AIR radiosonde relative humidity profiles, shown by the thick dashed lines, are compared to simultaneous Vaisala profiles (thick solid lines) measured 2 km south of the lidar site. The thin solid lines represent lidar profiles. Approximate observation times were: (a) 3 Sept., 1997, 0714 UTC, (b) 4 Sept., 0618 UTC, (c) 8 Sept., 0700 UTC, (d) 10 Sept., 0648 UTC, (e) 11 Sept., 0621 UTC, and (f) 27 June, 1200 UTC. The lidar site was located at 22.05 N, 159.78 W and Vaisala launches (a)–(e) were at 22.03 N, 159.78 W. In (f) the AIR sonde was from a different batch and the Vaisala profile was measured at 1533 UTC. The open black squares correspond to the Lihue NWS profile for 27 June, 1997 at 1200 UTC.

cloud tracks were observed at 2 km altitude. These usually dissipated in the early evening, prior to satellite overpass. Surface wind speed at PMRFK was generally 1–2 m/s, increasing to prevailing tradewind speed (6–10 m/s) at altitudes of 1–2 km. Wind direction frequently reversed to westerly at 5–8 km. During the September campaign, surface winds varied from westerly to northerly, whereas upper winds were westerly. The night sky was dark during most observation periods.

Surface temperature was close to sea surface temperature (26–27 °C) throughout the campaigns. Surface humidity varied from 50 to 75%. Cloud cover varied significantly during evenings and from night to night. Conditions were assessed on

the basis of lidar, DMSP OLS, GOES, and GMS mid-infrared imagery.

Radiative transfer (forward) calculations were applied to lidar and radiosonde data, providing comparisons with satellite observations. The model of Liebe and Layton [14]–[17] was used in conjunction with Fresnel surface emission based on water dielectric constant measurements presented by Ellison *et al.* [18] The forward calculation uses a simple in-house numerical integration program. Lidar measurements terminated at altitudes below the sensitive range of the upper troposphere microwave channels. Therefore, lidar profiles used in calculations were artificially extended by linearly extrapolating RH on an altitude scale from the highest reliable lidar measurement to the RH that is equivalent to 4 ppmv water vapor at the tropopause.

The SSM/T-2 instrument [19] is a five channel cross-track microwave radiometer. It has three channels centered on the 183.3 GHz water vapor band, each has dual sidebands, displaced by ±1, ±3, and ±7 GHz, representing upper, middle, and lower tropospheric water vapor, respectively. In addition, it has "window" channels at 150 and 92 GHz, which receive typical surface contributions of about 10 and 40%, respectively. The instrument derives in-flight calibration by viewing a thermostated blackbody emission source at one end of scan, and by viewing cold deep space at the opposite end of scan. Instrument specifications imply a calibration uncertainty of about 1K. The footprint for each channel depends on frequency and scan angle. At nadir, the 92 GHz channel footprint has a circular diameter (3 dB) of 85 km. This becomes elliptical at the outer beam position of 40.5°. The largest fractional projection of Kauai's surface on the 92 GHz footprint is 0.2. Footprint size is inversely related to frequency. However, the 183 GHz channels are not responsive to the surface in moist atmospheres, thus the high emissivity of land does not interfere with these channels. Over water, polarization must be taken into account for beam positions away from nadir in the window channels. The instrument measures a scan angle dependent mixed polarization given by

$$T_b(\text{mixed}) = T_b(h) \cdot \cos(\theta)^2 + T_b(v) \cdot \sin(\theta)^2 \qquad (5)$$

where

- h horizontal polarization;
- v vertical polarization;
- θ nadir angle.

Sources for satellite data included AFGWC, NOAA SAA [20] and a DMSP STT portable downlink terminal operated at PMRFK. OLS infrared data was acquired from the STT and from NGDC [21].

A. June–July Results

1) Measurement Characteristics: Fig. 3 presents typical lidar and radiosonde profiles for the first campaign. Dark current corrections ($DC(H_2O)$, $DC(N_2)$) were applied to the signals in order to achieve good fits between data at long ranges (after-pulse correction is not used in this figure). $DC(H_2O)$ was initially set equal to the average photon count number (about 1–5 counts per 12 m range bin for 15 000 pulses) in the interval from 14–16 km, where water vapor was unmeasurably low. It was then adjusted (by a factor as large as 2) in order

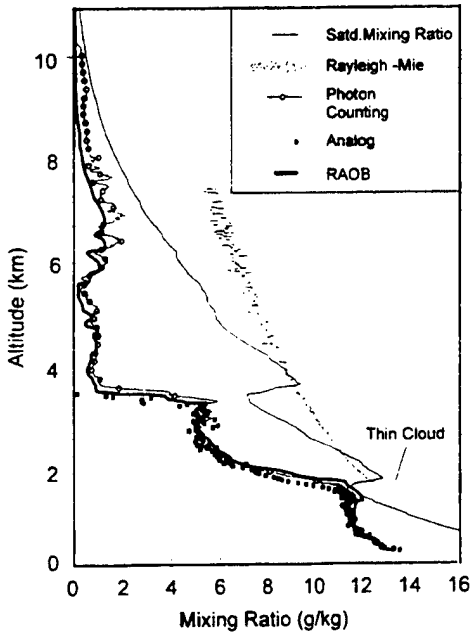

Fig. 3. Typical lidar and radiosonde water vapor mixing ratio profiles for 26 June, 1997, 0744 UTC. The thin solid line with open circles represent lidar mixing ratio measured from 2 to 10 km, the thick dark line is the AIR radiosonde, and gray squares represent the analog signal from 0.4 to 3.5 km. The Rayleigh–Mie channel (noisy gray line) reveals a thin cloud at 2 km altitude. The thin black line represents the saturated mixing ratio, determined from the radiosonde temperature profile.

to achieve a vanishing mixing ratio (4 ppmv) at 14 km. In most cases, lidar and radiosonde measurements matched well up to 6 km altitude. However, additional correction for photomultiplier after-pulsing was required for high accuracy, as discussed below. For full intensity measurements, as in Fig. 3, photon-counting data were highly distorted by pulse-pile-up effects for ranges less than 1.8 km, therefore only analog and radiosonde data are used below 2 km. The presence of intermittent thin clouds are revealed by a small peak in the Rayleigh–Mie channel near 2 km altitude, which provides negligible attenuation. Typically, little change was observed in the low altitude regime during 4 h observations. Changes were more pronounced at higher altitude. Above 6 km altitude, RH determined by lidar tended to be higher than that reported by AIR radiosondes (RAOB's).

Fig. 4 presents data recorded in the presence of thin cirrus clouds at 9 km altitude. In this typical case, the radiosonde did not report saturation at cloud level, whereas the lidar, which was adjusted to agree with the RAOB at 3–6 km, indicated a saturated mixing ratio (relative to ice) at the cloud base. Some lidar measurements indicated RH exceeding 100% inside or above high altitude clouds. This may represent supersaturation during cirrus formation [22]–[26] or it may be due to a measurement artifact associated with either increased attenuation of the nitrogen Raman signal relative to water Raman signal within the cloud, and/or leakage of Rayleigh–Mie scattering into the water channel. (In a few unrecorded cases, the nitrogen and water channel signals increased up to about 20% as the beam penetrated a cloud, when observed with the Barr filter set. This was not observed with the narrower bandwidth CVI filter set used in Fig. 4, although instances of apparent supersaturation occurred

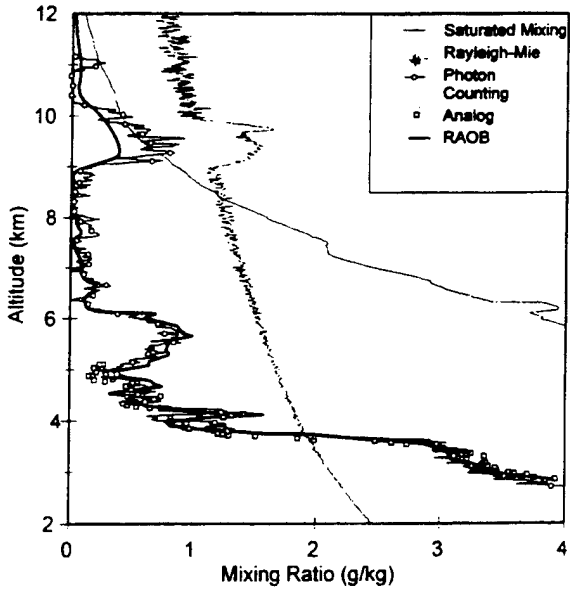

Fig. 4. Water vapor mixing ratio profiles are shown for 24 June, 0825 UTC as measured by AIR radiosonde (solid thick black line), photon-counting lidar (thin black line with open circles), and analog (lidar solid squares). A thin cirrus cloud induces Mie scattering (noisy gray line) at 9 km altitude. The saturated mixing ratio (MR) is the thin solid black line.

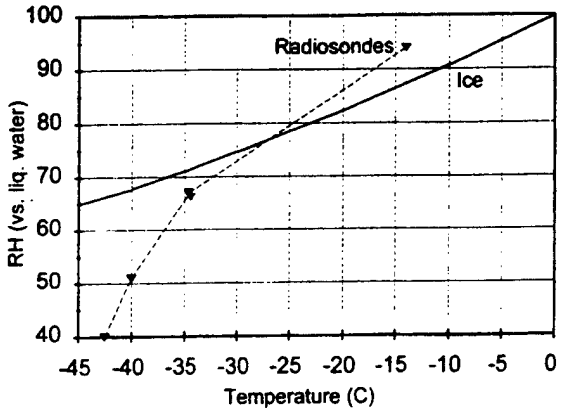

Fig. 5. Relative humidity (RH) measurements (solid black triangles) are plotted versus cloud temperature for five flights where the radiosondes penetrated high clouds. The relative humidity of the ice phase referenced to liquid water is shown for comparison.

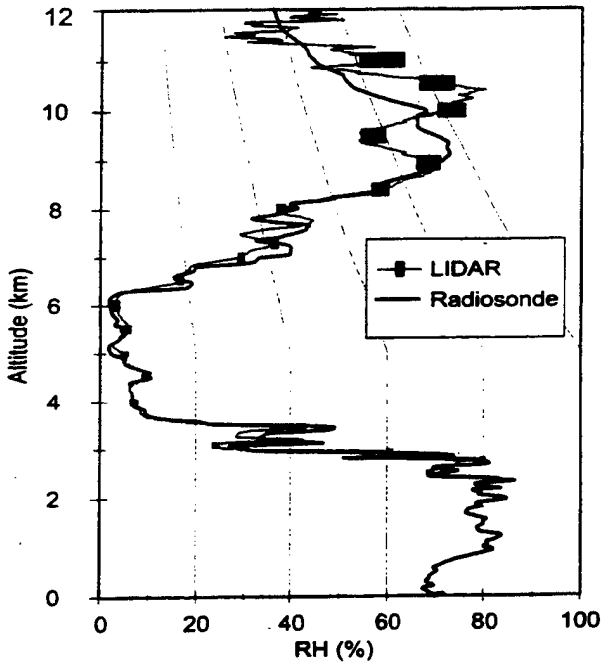

Fig. 6. Relative humidity profile for September 11, 1997, 0640 UTC derived from lidar (thin gray line) is compared with measurement by AIR radiosonde (thick black line). The widths of the rectangles are the statistical error estimate for lidar and the heights correspond to range bin averaging. The RMS difference between lidar and radiosonde RH over the range 2.7–9 km is about 2%. There is additional uncertainty in lidar-derived RH above 10 km associated with after-pulse correction and dark current baseline offset.

with both filter sets.) RAOB's typically varied, reporting from 40 to 60% RH within clouds above 6 km, which is shown for five nights in Fig. 5. The RAOB's failed to resolve structure in profiles above 9 km (<–25C). The large discrepancies are in the direction consistent with saturation over ice referenced to a liquid water vapor pressure curve (extrapolated below freezing temperature). In the September campaign, many radiosonde and lidar profiles agreed within about 2% in RH from 2.7 to 9 km altitude, as shown in Fig. 6, provided the lidar measurement time corresponded to the radiosonde altitude. In Fig. 6, the lidar profile was measured when the radiosonde was at 4 km altitude.

Lidar was used at varying elevation angles in order to improve low altitude measurements and to assess the horizontal variability of water vapor. No detectable difference in profiles was observed for elevations from 30 to 90°. Horizontal variations were on the order of 10–20%, with changes occurring over time intervals of 10–30 min.

For zenith pointing measurements, lidar signals were observed to have anomalous behavior at high altitude, such that background-corrected signals were elevated relative to the expected exponential decrease in water vapor. This is indicative of after-pulsing. For ratio signals, the anomaly was essentially independent of overall signal level. The effect was investigated in detail during the September campaign. As a result, forward calculations performed for the 183 ± 1 GHz channel data were less reliable in June–July than for September.

2) Comparison with Satellite Data: Forward calculations are compared to satellite data records (SDR's) in Table I. Although the profiles used for calculations for June and July, appearing on the left side of the table, were acquired before after-pulse correction was developed, they were corrected by post-processing. Generally, the correspondence between SDR's and calculations is excellent, except for surface sensitive 92 and 150 GHz channels. The 92 and 150 GHz discrepancies are similar for lidar and for radiosonde profiles. This is attributed to the fact that these channels respond to low altitude water vapor profiles (Fig. 1 insert), which were similar for the two methods. Upper tropospheric profiles were significantly different (Figs. 2 and 3) and this resulted in appreciable differences for the 183 ± 1 and 183 ± 3 GHz channels, (Table I) which are sensitive to upper tropospheric water vapor. At first, it was thought that acceptable agreement would be confined to relatively cloud-free nights. Later, it was established that agreement was excellent on most nights, provided after-pulse corrections were

TABLE I
SUMMARY OF ERRORS

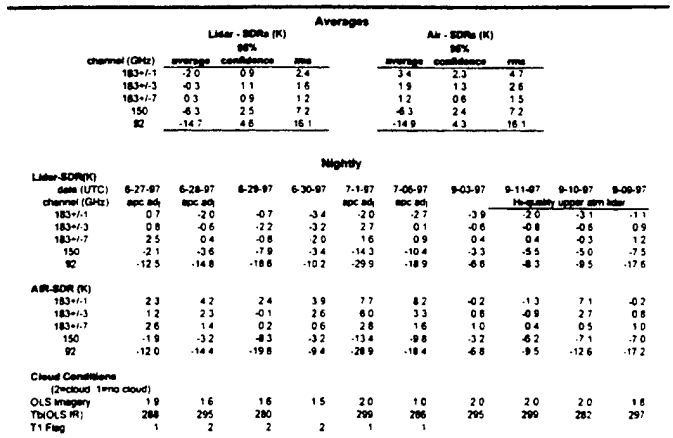

Averages

channel (GHz)	Lidar - SDRs (K) average	95% confidence	rms	Air - SDRs (K) average	95% confidence	rms
183+/-1	-2.0	0.9	2.4	3.4	2.3	4.7
183+/-3	-0.3	1.1	1.6	1.9	1.3	2.6
183+/-7	0.3	0.9	1.2	1.2	0.6	1.5
150	-6.3	2.5	7.2	-6.3	2.4	7.2
92	-14.7	4.8	16.1	-14.9	4.3	16.1

Nightly

Lidar-SDR(K) date (UTC)	6-27-97	6-28-97	6-29-97	6-30-97	7-1-97	7-06-97	9-03-97	9-11-97	9-10-97	9-09-97
channel (GHz)	apc adj	apc adj			apc adj	apc adj		Hi-quality upper atm lidar		
183+/-1	0.7	-2.0	-0.7	-3.4	-2.0	-2.7	-3.9	-2.0	-3.1	-1.1
183+/-3	0.8	-0.6	-2.2	-3.2	2.7	0.1	-0.6	-0.8	-0.6	0.9
183+/-7	2.5	0.4	-0.8	-2.0	1.6	0.9	0.4	0.4	-0.3	1.2
150	-2.1	-3.6	-7.9	-3.4	-14.3	-10.4	-3.3	-5.5	-5.0	-7.5
92	-12.5	-14.8	-18.6	-10.2	-29.9	-18.9	-6.6	-8.3	-9.5	-17.6
AIR-SDR (K)										
183+/-1	2.3	4.2	2.4	3.9	7.7	8.2	-0.2	-1.3	7.1	-0.2
183+/-3	1.2	2.3	-0.1	2.6	6.0	3.3	0.8	-0.9	2.7	0.8
183+/-7	2.6	1.4	0.2	0.6	2.8	1.6	1.0	0.4	0.5	1.0
150	-1.9	-3.2	-8.3	-3.2	-13.4	-9.8	-3.2	-6.2	-7.1	-7.0
92	-12.0	-14.4	-19.8	-9.4	-28.9	-18.4	-6.8	-9.5	-12.6	-17.2
Cloud Conditions (2=cloud 1=no cloud)										
OLS imagery	1.9	1.6	1.6	1.5	2.0	1.0	2.0	2.0	2.0	1.6
Tb(OLS IR)	288	295	280		299	286	295	299	282	297
T1 Flag	1	2	2	2	1	1				

made. SSM/T-2 imagery did not reveal the influence of land in the vicinity of Kauai, therefore land does not account for the surface discrepancies. Land area is too small relative to the 92 GHz footprint. Land and orographic clouds clearly influence the 92 GHz channel in the vicinity of the large island, Hawaii.

Surface sensitive channels are also susceptible to wind-induced ocean roughness. Several buoys monitor surface winds near the Hawaiian Islands. Wind speeds were relatively low and constant during the lidar campaigns. The effect of wind-induced roughness is considered in a following section.

B. September Campaign

1) Measurement Characteristics: During this period attention centered on improving high altitude water vapor measurements. A series of experiments tested the effect of central aperture obscuration. The intention was to discriminate against intense low altitude signals, while preserving weak high altitude signals. In addition, comparative measurements were made in the presence and absence of low altitude clouds, and a high-speed liquid crystal electro-optic shutter was implemented in order to attenuate low altitude signals.

Central obscuration experiments were inconclusive. Opaque disks of varying outside diameter blocked direct rays from low altitudes from reaching the primary mirror. Ratio measurements were not highly sensitive to the obscuration, however the overall signal levels declined as the clear aperture decreased. The measurements indicated that the low altitude signals are not significantly contaminated by spurious scattering from telescope components.

On several evenings, thick low clouds drifted in and out of view during observations. This was exploited in order to determine the effect of the intense low altitude signals on the high altitude measurements. Cases were examined in which Rayleigh and nitrogen channels indicated optically thick clouds. In these situations, signals should be essentially zero for range bins beyond clouds where a thick cloud cuts off signals beyond 2 km altitude. In every case, slowly decaying signals were recorded in water range bins above cloud level, as shown in Fig. 7. The waveform of the spurious signals was stable and the shape was

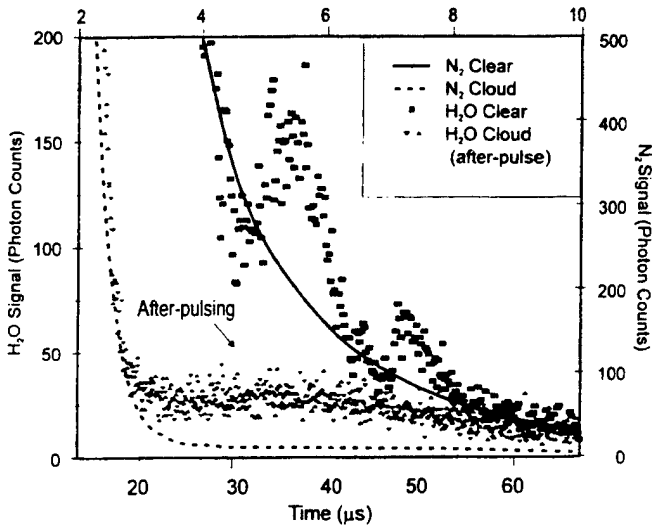

Fig. 7. After-pulse signals observed in the presence of an optically thick cloud at about 2 km altitude. Nitrogen Raman signals are shown in the absence (thick solid line) and presence (thick dashed line) of the cloud for reference. Two separate water vapor channel measurements are superimposed in the data labeled after-pulsing (small triangles). The water vapor signal recorded 15 min earlier under clear conditions is also shown.

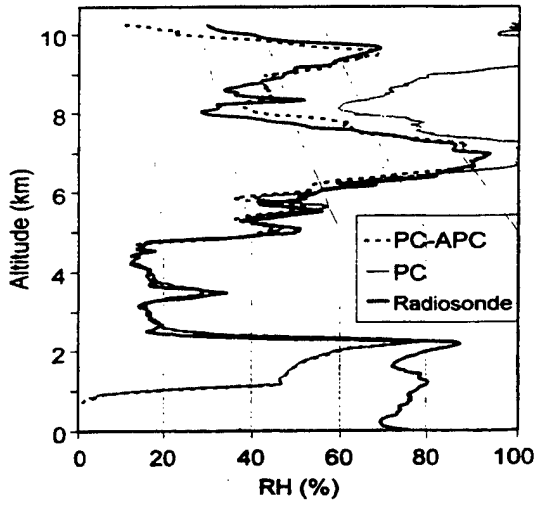

Fig. 8. An after-pulse corrected profile (dashed line) with a cloud at 7 km is compared to the uncorrected signal (thick gray solid line) and to an AIR radiosonde profile (solid black line) obtained September 6, 1997, 0800 UTC.

relatively independent of signal level (adjusted with neutral density filters), and of cloud altitude (below 4 km). The waveform (averaged over 0.1–0.5 km increments of the H_2O channel signals in the presence of clouds) was used for after-pulse correction of measurements made without electro-optic gating. The correction is significant, relative to average cloud-free water vapor signals, beyond 5 km range. The AP-corrected signals generally had correct asymptotic behavior and in all cases, correct saturated mixing levels were indicated at the bases of high thin clouds. Fig. 8 presents a typical example of an AP-corrected profile in the presence of a thin cirrus cloud. The figure also shows an uncorrected profile, which indicates the importance of the correction. (It should be noted, that the correct asymptotic behavior requires somewhat arbitrary adjustment of C_2, the AP waveform multiplier.) The data correction procedure consisted

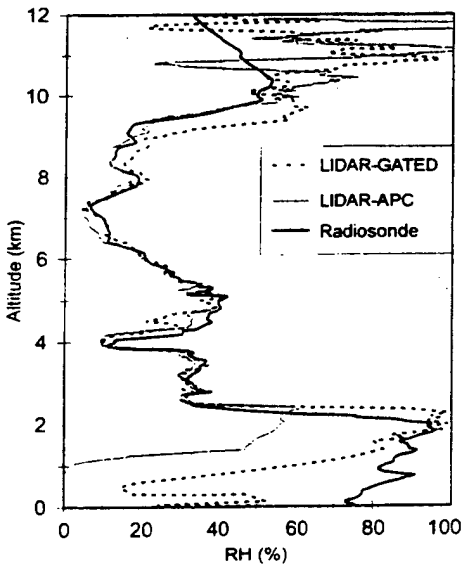

Fig. 9. The gray solid line represents an after-pulse corrected profile from September 12, 1997, 0630 UTC, in which the correction is scaled to give 100% RH (relative to ice) at the 10.3 km cloud base. The dark-current background correction is measured from the average 23–24 km water signal. This results in a good "natural" match to clouds observed at 11.2 and 11.8 km. The dashed line corresponds to data obtained 23 min later using the electro-optical shutter. In this case, there is no AP correction and dark-current background is from the 23–24 km signals. The gated measurement indicates 100% RH at the 2 km and 10.9 km clouds. The shutter opens fully at about 3 km and switching transients occur from 0 to 2 km.

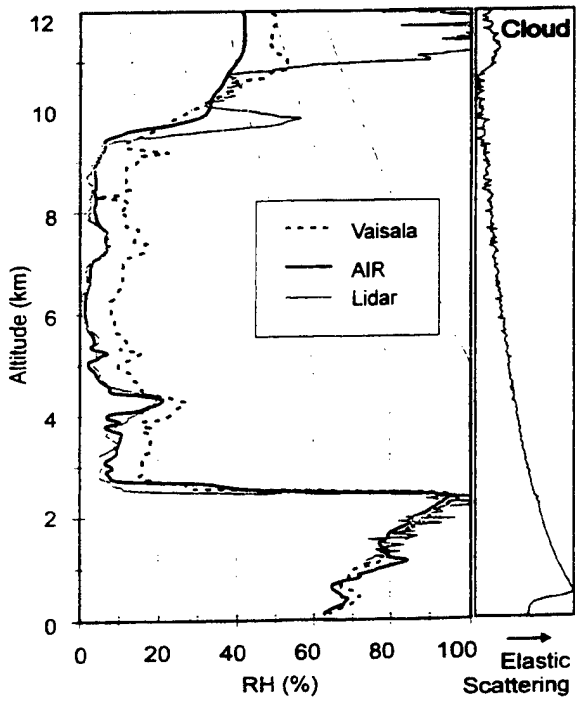

Fig. 10. Comparison of AIR, Vaisala, and lidar profiles on September 10, 1997, 0800 UTC, in the presence of a thin cirrus cloud at 11 km. The lidar profile is AP-corrected, where the scaling constant is taken from the 14–20 km signal.

of subtracting the dark current correction [setting $DC(H_2O)$ in (1) equal to the average signal amplitude for 20–24 km altitude] and then subtracting the AP waveform which was scaled by setting C_2 equal to the ratio of the average signal over the range 14–15 km divided by the amplitude in the AP waveform. Small additional adjustments were made in C_2 in order to minimize the RMS difference between lidar and radiosonde profiles in the range 3–6 km and finally, the dark current correction was readjusted to achieve convergence to zero water vapor above 14 km. The same procedure improved data obtained at reduced intensity (1.0 and 2.0 units of neutral density added to the optical train).

Uncertainties associated with AP correction were reduced by use of an electro-optic shutter. Results are illustrated in Fig. 9. The ratios are not corrected for wavelength and time dependent retardation at short times following the on-pulse for the device. Therefore, ratio measurements are only reliable beyond 2 km. Measurements obtained with the electro-optic shutter are nearly free of the slowly decaying AP waveform. Nonetheless, a small AP correction (10% of that needed in the absence of the shutter) improved the agreement between lidar and AIR RAOB's over the range from 7 to 9 km. The gated measurements at long range were generally similar to those made without a gate using optimized AP corrections. The shutter was not used routinely because it attenuated the water signals by about 80% in the open state.

Fig. 10 represents a case where the lidar signal revealed a high altitude cirrus cloud and the AP-corrected data provided a convincing fit to the AIR data for 3–9 km. The AP correction leads to saturation at cloud level, whereas the AIR and Vaisala radiosondes reported lower RH. The right hand panel shows the logarithm of the Rayleigh–Mie (elastic) signal multiplied by range^2.

The Vaisala profile in Fig. 10 is significantly moister than AIR and lidar profiles for altitudes from 3 to 9 km. This is a persistent trend in the September data sets, whenever RH declines below 20%. It accounts for the poorer correspondence between forward calculations and SDR's for Vaisala radiosondes. AIR values in this regime are assumed to be more reliable because they report changes in RH with altitude in close agreement with changes in the lidar signals. Lidar measures changes accurately over this range. Although the same general features are present in Vaisala profiles, the magnitude of the changes is inconsistent with lidar. If the lidar constant is adjusted to provide minimum RMS with respect to the Vaisala curve, RMS increases fourfold and relative humidity (liquid water) greatly exceeds 100% at cloud level. The segments of the Vaisala profiles in question are in excellent agreement with lidar and AIR if a 7% RH baseline is subtracted from the segments of the Vaisala profiles with low RH at altitudes between 3 and 9 km. Similar behavior was observed in all September midaltitude profiles for RH below 20%. Although there is a 7–8 h time interval between AIR and Vaisala flights of June–July, the data have similar tendencies.

Even though low altitude profiles were relatively stable over periods of 2–4 h in September, fine structure varied rapidly, particularly from 2 to 6 km. Night-to-night variations were large, except that a stable boundary layer was common at 2 km. Profiles above 6 km were more variable. On some evenings, variations occurred on time scales of 10–15 min, providing evidence of rapidly changing layer structure, as shown in Fig. 11 for the

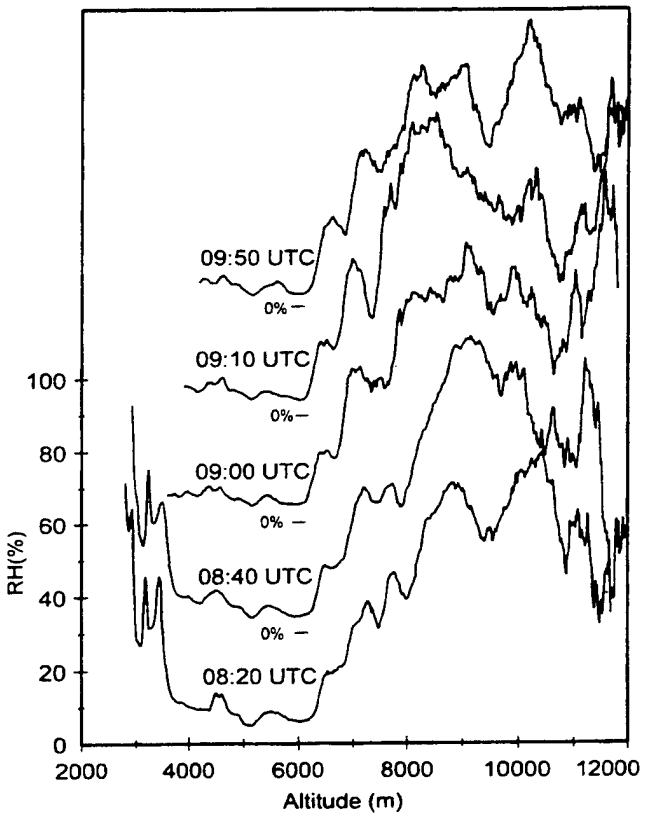

Fig. 11. Series of RH profiles recorded on September 11, 1997 UTC. Curves at 08:20 and 08:40 were measured directly, with AP correction. An electro-optical shutter was employed in subsequent measurements, therefore these are reliable, although noisy above 10 km. The RH scale applies to the 08:20 curve and each succeeding curve is offset additionally by 30% RH.

upper troposphere. On other evenings, the entire atmosphere was stable.

2) Comparison with Satellite Data: Time dependence of forward calculations was investigated with data recorded on September 11, 1997Z when both AIR and Vaisala radiosondes were flown. Fig. 12 shows that the largest changes are calculated for the mid-troposphere ±3 GHz channel. The change at 70 min can be related to the change in the 9:10Z profile in Fig. 11 where RH increases significantly at 8 km. This change substantially exceeds experimental uncertainty. The ±1 channel changes less because its weighting function (Fig. 1 insert) is peaked at higher altitude. Calculations for this channel are uncertain because the RH calculations in Fig. 11 are highly sensitive to dark current corrections for altitudes above 10 km, which contribute to ±1 response. Stability of the ±7 channel calculations reflects the lack of change in profiles from 2 to 7 km. Fig. 12 indicates agreement with the radiosondes is reasonably good for all the atmospheric channels.

Forward calculations, based on the September measurements, are in excellent agreement with the SDR's, except for surface sensitive channels. On average, as shown in Table I, the 92 GHz discrepancy is 15K with the calculated values being low. 150 GHz discrepancies were smaller and in the same direction. The few instances with significant discrepancies in the atmospheric channels correlate with the presence of thick upper atmosphere clouds, based on OLS and surface observations.

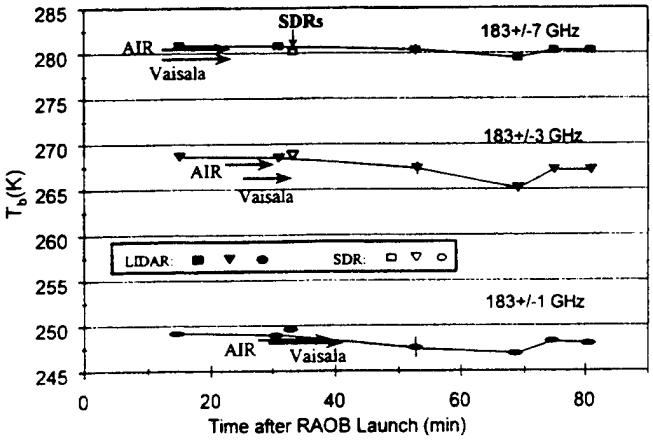

Fig. 12. Time series forward calculations on September 11, 1997 UTC. The horizontal arrows represent forward calculations based on AIR and Vaisala radiosondes, and their horizontal positions represent the approximate times when the radiosonde altitudes corresponded to the peak of the weighting function for the displayed channel. The thin vertical lines at 53 min represent the estimated geographic spread of the SDR's in the vicinity of PMRFK.

III. Discussion

A. High Altitude Discrepancies

On five nights, radiosondes that passed through high altitude clouds failed to reach 100% RH. The radiosonde measurements lack structure in the vicinity of the clouds, whereas lidar indicated appreciable structure. The RH discrepancy above 10 km exceeds the ice/liquid water phase ambiguity. Humidity sensors become relatively unresponsive at temperatures below −25 °C to −32 °C, whereas prior work suggested problems occur below about −35 °C [4]. Fig. 5 illustrates the RH measurement problem as a function of cloud level temperature for AIR radiosondes on five nights.

Forward calculations based on lidar data accurately predict SDR's observed in the atmospheric channels, provided photomultiplier after-pulsing is taken into account. For a given instrumental setup, it is possible to correct for this effect by scaling an after-pulse waveform to the integrated amplitude of the signal. The after-pulse waveform can be obtained in the presence of thick low cloud cover. The effect can also be deduced from signals recorded using an electro-optic shutter which attenuates close range (high amplitude) signals.

B. Low Altitude Discrepancies

1) Orographic Effects: A large discrepancy (Table I, Fig. 13) occurs between forward calculations and the 92 GHz Kauai SDR's, whereas substantial agreement [8], [27] was reported in prior work involving downward microwave radiometry from aircraft over an ocean surface. The discrepancies in the Kauai results are nearly identical when calculated for either radiosonde or lidar measurements, as is expected because the 92 GHz measurements are dominated by low altitudes where the two methods yield similar data. Direct upward radiated atmospheric signals account for about 60% of the signal at 92 GHz and about 90% of the 150 GHz signal. The weighting is, about equal for all altitudes, therefore contributions to T_bs are essentially proportional to water vapor density. As a consequence, forward calculations are insensitive to structure

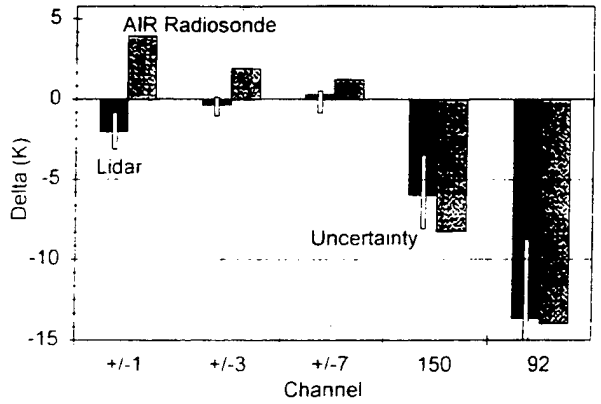

Fig. 13. Average discrepancies between forward calculations based on lidar and SDR's (black) and between calculations for AIR radiosondes and SDR's (gray). The thin rectangles represent uncertainties (95% confidence) based on variation of discrepancies.

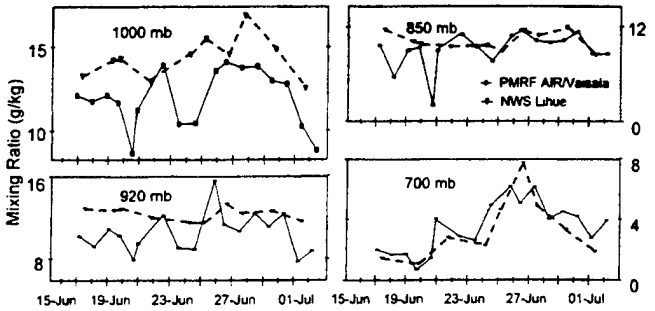

Fig. 14. Comparison between RH reported by NWS from Lihue with AIR radiosonde measurements at PMRFK at the 1000, 920, 850, and 700 mb levels.

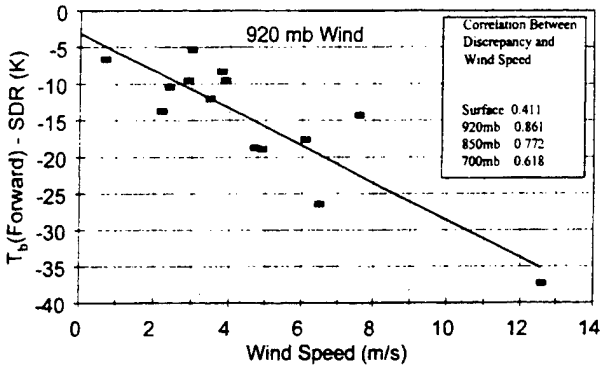

Fig. 15. Discrepancy at 92 GHz (forward calculation minus SSM/T-2 observation) versus wind speed. The line represents a linear least squares fit to the data.

or small errors in portions of the profiles, but they do vary with total integrated water. A 15% increase in integrated water increases $T_b(92)$ by about 15K and $T_b(150)$ by about 7K for the average profile, which are comparable to the observed discrepancies. However, this humidity increment is about three times the uncertainty in the measured profiles.

The 92 GHz Kauai imagery was examined for local topographic effects. Such effects were absent at 92 GHz near Kauai, which occupies a maximum of 20% in the T-2 footprint. However, the influence of orographic clouds was evident in the case of Hawaii, which is both larger and higher. Additional evidence for an orographic effect was sought in differences between water vapor profiles reported in Lihue and PMRFK. These sites are separated by 44 km. PMRFK was on the leeward side of Mt. Waialeale during June–July, whereas, Lihue had direct exposure to offshore tradewinds. Average surface water vapor differs significantly between the two sites in June–July, with drying at PMRFK (Lihue measurements occurred ~4 h later than PMRFK). At 1000, 920, and 850 mb PMRFK RH's are, on average, 82, 84, and 86%, respectively, of those reported at Lihue. The relative drying vanishes at 700 mb. The nightly values are compared for different levels in Fig. 14, where the dashed line represents values at Lihue and the thin solid line represents PMRFK values.

The effect of drying was estimated by performing forward calculations. On average, drying is expected to reduce the calculated 92 GHz T_b by 9 ± 4K, compared with the average discrepancy between calculations and SDR's of 14.7 ± 4.6K.

2) Surface Roughness: The effect of ocean surface roughness on window channel brightness temperatures was modeled in order to further resolve the discrepancy. The geometrical optics model of Stogryn [28] and Wilheit [29] was applied to the 92 GHz data. On average, ocean surface winds were mild, about 8.8 ± 2 m/s (10 m above the surface). This is a regime where modeling is expected to be relatively accurate. The model predicts that winds increase brightness temperatures by 2 ± 1K on average for the range of earth incidence angles (0–0.9 radian) that apply to SSM/T-2. This is negligible with respect to the observed 15K discrepancy.

The 92 GHz discrepancies were examined for correlation with winds. Correlation was low (0.411) for surface wind, however, as shown in Fig. 15, it is highly significant (0.861) for 920 mb wind (about 1 km altitude). This supports the orographic drying hypothesis. A linear least squares fit to the data in Fig. 15 has a zero wind speed intercept of –3K, which is in the direction predicted by the surface roughness, although the intercept is less than the uncertainty in the extrapolation. Smaller discrepancies occur at 150 GHz because this channel samples less from the surface.

Collocated data from the SSM/I microwave imager radiometer were examined in order to investigate the orographic drying hypothesis and confirm window channel measurements from SSM/T-2. The 19 and 37 GHz SSM/I channels are relatively insensitive to variations in water vapor, whereas they are highly sensitive to surface conditions. Previously, investigators reported that forward calculations applied to radiosonde data over smooth ocean water were in excellent agreement with SSM/I measurements ($19h + 2$K, $37h + 6$K, $85h + 2$K, $19v + 4$K, $22v + 4$K, $37v + 6$K, $85v - 3$K relative to SDR's) [27]. For Kauai data, large discrepancies occur for most of the horizontally polarized measurements. These are, on average, 23K higher than calculated for smooth ocean surfaces for all SSM/I horizontal frequencies. The vertical measurements are about 5K higher than calculated. These trends are consistent with an analysis of SSM/I oceanic wind data described by Rosenkranz [30]. He derived the wind speed dependence for corrections to emissivities for low wind speeds. The corresponding corrections for Kauai data at the average wind velocity of 8.8 m/s account for 15.5K warming at 19 and 37 GHz horizontal channels and 9.3K for 85 GHz horizontal channel.

His data also suggest much smaller changes for the vertically polarized channels.

SSM/I provides higher resolution imaging than T-2; therefore, water column retrieval algorithms were applied to the SSM/I data to test the hypothesis of local orographic drying on the leeward side of Kauai. No effect was observed, however the maximum resolution was about 20 km in the 22 GHz channel, which is highly sensitive to columnar water. SSM/I data sets were examined for azimuthal dependence, which modeling predicts [31], can produce differences as large as observed, for a narrow range of angles. Prevailing wind directions were well known from buoy reports and azimuth angles varied across swaths and from pass to pass. The horizontal discrepancy was not significantly related to the satellite-wind azimuth.

The frequency independent discrepancies suggest a uniform emissive surface coverage such as foam or random small scale roughness may be influencing the measurements. Data were modeled in terms of a contribution from a smooth Fresnel surface and from fractional coverage by a unit emissive layer. Fractional coverage was adjusted to give the best RMS fit between forward calculations and SDR's for each frequency. Fractional coverage of 0.24, 0.12, 0.09, and 0.1, respectively, provided the best RMS fits to the 85, 37, 22 and 19 GHz data, reducing the average RMS error from 15.5 to 4K averaged over all channels. The requirement for frequency dependent fractional coverage is not easily explained in terms of foam coverage, which is expected to be insignificant at prevailing wind speeds. Instead, it is more likely that the discrepancies are caused by Bragg scattering from fine scale random roughness. Gravity-capillary waves, as discussed by Apel [32], and measured by Klinke and Jahne [33] and Jahne and Riemer [34] in radar backscatter studies have spectral amplitudes approximately dependent on the square root of roughness wave number over the range sensed by the SSM/I channels. This matches the frequency dependence derived from the best fit to the SSM/I discrepancy data. The Bragg scattering contribution is described in the literature [35], [36]. The cited radar measurements include large azimuthally independent hh backscatter cross sections, which is suggestive of random roughness and entirely consistent with the SSM/T-2 and SSM/I Kauai surface observations. The Kauai SSM/I data require, at minimum, a three component roughness model in which the ocean surface is covered inhomogeneously with RMS roughness height variations of 1, 3.5, and 15.5 mm with weights of 0.8, 0.1, and 0.1, respectively. This model reduces discrepancies in the available SSM/I data from 14K to 4K and explains lack of azimuthal angle dependence for SSM/I and scan angle independence for SSM/T-2 discrepancies.

3) Clouds: Evidence for cloud-induced discrepancies between the microwave and lidar-based measurements was sought. On several nights, OLS imagery revealed extensive cumulus cloud coverage and precipitation was evident from PMRFK ground observations. In these cases, deviations between forward calculations and SDR's were large and the data were rejected for calibration purposes. Precipitation probably accounted for the primary discrepancies. In the most severe cases, the errors occurred in all channels. On most evenings OLS and GMS imagery indicated scattered or low altitude

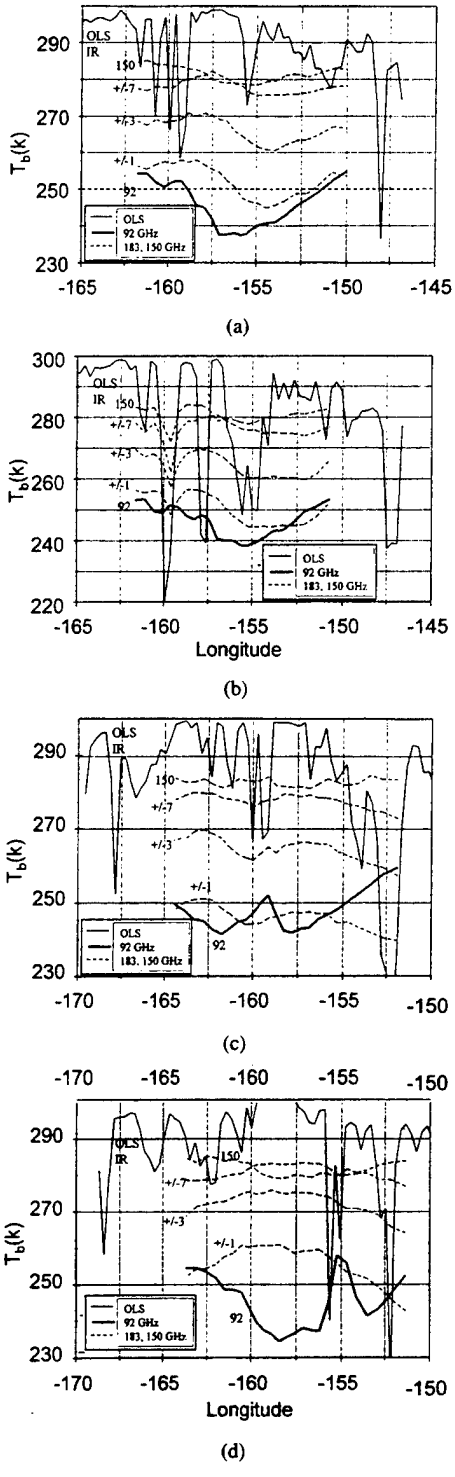

Fig. 16. Comparison between co-located scans of SSM/T-2 and OLS midinfrared: (a) on September 22, 1997, 0818 UTC at 22N (Kauai, 159.5W), (b) September 22, 1997, 0818 UTC, 21.2 N (Oahu, 157.9 W), (c) July 2, 1997, 0614 UTC at 22 N, (Kauai, 159.5 W), and (d) July 2, 1997, 0614 UTC, 19.7 N, (Hilo, 155.1 W).

clouds and there was no correlation between these clouds and the 92 GHz discrepancy.

Fig. 16 presents comparisons between collocated OLS midinfrared imagery and SSM/T-2 microwave signals observed near Hawaii. In most cases the correlation was weak between cloud features in the infrared and perturbations in the 92 GHz data. In Fig. 16(a) the 92 GHz channel increases in brightness

temperature near the clouds over Kauai at 159–161 W, whereas clouds are indicated by decreases in the infrared T_bs. Horizontal resolution is about 1° at 92 GHz, therefore, if T-2 were sensitive to cloud scattering, sharp structure would appear in the microwave imagery. Instead, 92 GHz brightness increases gradually, which is consistent with increasing water vapor at low altitude. Also, there are no discrete microwave features in the vicinity of 156 W, where a medium altitude cloud appears in the midinfrared OLS scan. The 183 GHz channels provide spatial resolutions of ~0.5°, which is comparable to the smoothed OLS data in Fig. 16. Whereas, brightness temperatures are expected to decline near the edge of scan for a uniform atmosphere in the 183 GHz channels, Fig. 16(a) shows a mild increase, which indicates a drying of the upper atmosphere to the west. The significant increase in the 92 GHz brightness in this direction suggests an increase in low altitude water vapor, which is supported by the slow decline of OLS brightness associated with low altitude clouds. Fig. 16(b) corresponds to a scan across Oahu. A cold cloud appears near 160 W and the 183 GHz channels respond with sharp features indicating a highly scattering cirrus ice cloud. The 92 GHz channel is less affected, possibly due to reduced scattering at the lower frequency, or due to the reduced temperature difference between the cloud and the surface signal in this channel. Significant OLS cloud structure occurs at 155 W without corresponding microwave structure. The ±1 and ±3 channels decrease in brightness going from 158 to 155 W, representing the increased water vapor that supports the high altitude cloud formation, shown in the OLS imagery. OLS in Fig. 16(c) shows typical orographic cloud structure over Kauai. The corresponding increase in 92 GHz brightness near Kauai is too large to represent the influence of high land emissivity. It suggests upwelling of surface moisture, starting abruptly to the east of Kauai. It also displays a gradual increase in brightness to the east, reaching a high value at the edge of scan, indicating large amounts of low altitude water vapor. The corresponding OLS scan reveals the build-up of massive cloud structure in this direction, starting with low altitude clouds and terminating with thick high cirrus. The 183 GHz channel signals are consistent with upper atmosphere water vapor gradually increasing to the east. Fig. 16(d) was recorded in the vicinity of Hawaii. The OLS channel has a strong response to clouds over the island at 155 W, and 92 GHz rises abruptly, responding to either orographic moisture and/or to the significant land area of the island. As in other cases, the 183 GHz channels are insensitive to this feature, therefore high altitude scattering is unimportant. The region from 157 to 160 W represents clear conditions, in that the OLS signal attains the surface brightness temperature. Correspondingly, the 92 GHz channel reaches the low temperatures predicted by forward calculations for relatively dry tropical atmospheres. When this channel approaches 250K, going west from 160 W, the lower atmosphere is very moist. OLS shows the effect of low altitude clouds in this region (brightness temperature ~280K). The eastern edge of this scan reveals a high altitude cloud, which is consistent with the massive upper altitude build-up of moisture indicated by the 183 ± 1 and ±3 channels. The decline in brightness in the easterly direction in these channels is gradual and does not have the sharp structure associated with the cloud scattering in the OLS trace.

These observations indicate that the microwave signals are not sensitive to ice-free nonprecipitating clouds in the vicinity of Hawaii. Discrepancies averaged over nonprecipitating cloud regions near Hawaii were about the same as for data measured under the cloud-free conditions. Therefore, we conclude that it is not necessary to screen microwave data from scenes involving typical scattered marine clouds in the vicinity of Hawaii.

IV. Conclusion

For atmospheric channels, agreement between lidar and microwave data is considerably better than for radiosonde-based data. AIR radiosonde and lidar measurements are in substantial agreement up to 6 km, therefore the radiative transfer results are similar for the 150 and 92 GHz window channels. Improved agreement between lidar and the atmospheric channels is probably due to increased accuracy in the 6–11 km range and to improved temporal sampling. In the case of lidar, predictions for the middle tropospheric channels are within 0.3K of the corresponding measurement averages. This is better than the specified internal calibration accuracy of SSM/T-2. The discrepancy between lidar and microwave degrades to −2K for the highest channel. This is larger than the statistical errors in the lidar measurements and may be due to bias above 12 km, where an artificially estimated RH profile is used in place of vanishingly small lidar signals. The much larger discrepancies (−14.7 and −6.3K) for the surface sensitive 92 and 150 GHz window channels are statistically significant and are provisionally attributed to Bragg scattering from random surface roughness associated with gravity-capillary waves and possibly, partly due to orographic drying in the vicinity of the lidar.

It will be necessary to study the relationship between infrared and microwave signals in greater detail in order to test the hypothesis that nonprecipitating clouds have a small effect on typical marine microwave measurements. In this study, three of the ten "reliable" measurement sets were made under cloud flagged conditions and the discrepancies for this subset were within statistical fluctuations of the reliable data set. If this conclusion is applicable at the high frequencies of SSM/T-2, it implies that nonprecipitating clouds are even less problematic for SSM/T-1 and SSM/I. Finally, additional efforts are needed to evaluate the importance of horizontal and temporal variability.

Unreliable radiosonde data represents a persistent problem. These studies, combined with prior published experience, suggest that both random and systematic errors are common. Furthermore, the systematic errors can change from batch to batch of radiosondes. However, we believe that reasonably accurate lidar calibration can be derived by selecting physically reasonable radiosonde data, for example, measurements attaining saturation at cloud bases, and demanding that the amplitude variations in profile structure correspond to the changes observed in lidar where lidar response is linear.

For the Kauai experiments, the RMS difference between the reliable AIR and lidar measurements for altitudes 2–6 km corresponds to ~2% RH. Although our radiosonde data appears to be unreliable above 9 km, it was possible to extend measurements to higher altitude using lidar. This was based on the observation that the lidar constant is stable and independent of altitude. The accuracy required to calibrate SSM/T-2 atmospheric channels is based on this capability. Additional studies are needed to resolve the surface channel discrepancies.

ACKNOWLEDGMENT

The authors would like to express appreciation to supporting staff for design, construction, and deployment activities. Particularly important contributions were made by D. Hinkley, J. Skinner, S. LaLumondiere, and for deployment, M. Zellmer and the Hawaiian Air National Guard. Thanks are also due to Dr. C. Selvey, A. Kishi, D. Boucher, Lt. L. Wilson, and Pfc. S. Pogozelski for important supporting efforts. Generous advice provided by Dr. H. Melfi and coworkers and by Dr. N. Grody is gratefully acknowledged. Informative comments from two referees substantially improved the manuscript.

REFERENCES

[1] D. J. Boucher, B. H. Thomas, and A. M. Kishi, "Performance of the DMSP SSM/T-2 microwave radiometer: A comparison between sensor derived, model analyzed, and radiosonde measured moisture variables," in *73rd Annu. Meeting, Amer. Meteorol. Soc.*, Anaheim, CA, Jan. 1993, pp. J150–J152.

[2] J. R. Wang, P. Racette, L. A. Chang, V. Falcone, M. Griffin, J. Pickle, and S. L. Moore, "Profiling of atmospheric water vapor with MIR and SSM/T-2 measurements," in *Int. Geoscience and Remote Sensing Symp., IGARSS'95*, vol. 2, T. I. Stein, Ed., New York, New York, 1995, pp. 1398–1400.

[3] V. J. Falcone *et al.*, "SSM/T-2 calibration and validation data analysis," in *Phillips Laboratory TR 92-2293*, MA, Nov. 1992.

[4] F. Schmidlin and J. Johansson, "Atmospheric moisture experiments: A microwave radiometer-radiosonde comparison," *IEEE Trans. Geosci. Remote Sens.*, vol. 31, pp. 389–398, 1993.

[5] A. Ansmann, M. Riebesell, U. Wandinger, C. Weitkamp, E. Voss, W. Lahmann, and W. Michaelis, "Combined Raman elastic-backscatter LIDAR for vertical profiling of moisture, aerosol extinction, backscatter, and LIDAR ratio," *Appl. Phys.*, vol. B55, pp. 18–28, 1992.

[6] R. A. Ferrare, S. H. Melfi, D. N. Whiteman, K. D. Evans, F. J. Schmidlin, and D. O'C. Starr, "A comparison of water vapor measurements made by Raman lidar and radiosondes," *J. Atmos. Ocean. Technol.*, vol. 12, pp. 1177–1195, 1995.

[7] Y. Han, J. B. Snider, E. R. Westwater, S. H. Melfi, and R. A. Ferrare, "Observation of water vapor by ground-based microwave radiometers and Raman lidar," *J. Geophys. Res.*, vol. 99, no. D9, pp. 18 695–18 702, 1994.

[8] J. R. Wang, S. H. Melfi, P. Racette, D. N. Whiteman, L. A. Chang, R. A. Ferrare, D. K. Evans, and F. J. Schmidlin, "Simultaneous measurements of atmospheric water vapor with MIR, Raman lidar, and rawinsondes," *J. Appl. Meteorol.*, vol. 34, pp. 1595–1607, 1995.

[9] D. Kley, H. G. J. Smit, H. Vomel, H. Grassl, V. Ramanathan, P. J. Crutzen, S. Williams, J. Meywerk, and S. J. Oltmans, "Tropospheric water-vapor and ozone cross-sections in a zonal plane over the central equatorial Pacific Ocean," *Q. J. R. Meterol. Soc.*, vol. 123, pp. 2009–2040, 1997.

[10] L. Campbell, "Afterpulse measurement and correction," *Rev. Sci. Instrum.*, vol. 63, pp. 5794–5798, 1992.

[11] H. S. Lee, G. K. Schwemmer, C. L. Korb, M. Dombrowski, and C. Prasad, "Gated photomultiplier response characterization for DIAL measurements," *Appl. Opt.*, vol. 29, pp. 3303–3315, 1989.

[12] C. M. Penney and M. Lapp, "Raman-scattering cross sections for water vapor," *J. Opt. Soc. Amer.*, vol. 66, no. 5, pp. 422–425, 1976.

[13] P. S. Anderson, "Mechanism for the behavior of hydroactive materials used in humidity sensors," *J. Atmos. Ocean. Technol.*, vol. 12, pp. 662–667, 1995.

[14] H. J. Liebe and D. H. Layton, "Millimeter-wave properties of the atmosphere: Laboratory studies and propagation modeling,", Boulder, CO, NTIA Report 87-224, Oct. 1987.

[15] H. J. Liebe, "An updated model for millimeter wave propagation in moist air," *Radio Sci.*, vol. 20, no. 5, pp. 1069–1089, Sept./Oct 1985.

[16] ——, "MPM—An atmospheric millimeter wave propagation model," *Int. J. Inf. Millim. Waves*, vol. 10, no. 6, pp. 631–650, 1989.

[17] H. J. Liebe, P. W. Rosenkranz, and G. A. Hufford, "Atmospheric 60 GHz oxygen spectrum: New laboratory measurements and line parameters," *J. Quant. Spectrosc. Radiat. Transf.*, vol. 48, no. 5/6, pp. 629–643, 1992.

[18] W. Ellison, A. Balana, G. Delbos, K. Lamkaouchi, L. Eymard, C. Guillou, and C. Prigent, "New permittivity measurements of seawater," *Radio Sci.*, vol. 33, no. 3, pp. 639–648, 1998.

[19] N. C. Grody, *Atmospheric Remote Sensing by Microwave Radiometry*, M. A. Janssen, Ed. New York: Wiley, 1993, pp. 264–311.

[20] NOAA Satellite Active Archive (1998). *http://www.sit.saa.noaa.gov* [Online]

[21] NOAA National Geophysical Data Center, DMSP Archive (1998). *http://www.ngdc.noaa.gov/dmsp/dmsp.html* [Online]

[22] A. J. Heymsfield and L. M. Miloshevich, "Relative humidity and temperature influences on cirrus formation and evolution: Observations from wave clouds and FIRE-II," *J. Atmos. Sci.*, vol. 52, pp. 4302–4326, 1995.

[23] A. J. Heymsfield, L. M. Miloshevich, C. Twohy, G. Sachse, and S. Oltmans, "Upper-tropospheric relative humidity observations and implications for cirrus ice nucleation," *Geophys. Res. Lett.*, vol. 25, no. 9, pp. 1343–1346, 1998.

[24] E. J. Jensen, O. B. Toon, A. Tabazadeh, G. W. Sachse, B. E. Anderson, K. R. Chan, C. W. Twohy, B. Gandrud, S. M. Aulenbach, A. Heymsfield, J. Hallett, and B. Gary, "Ice nucleation processes in upper-tropospheric wave clouds observed during SUCCESS," *Geophys. Res. Lett.*, vol. 25, no. 9, pp. 1363–1366, 1998.

[25] A. J. Heymsfield, R. P. Lawson, and G. Sachse, "Growth of ice crystals in a precipitating contrail," *Geophys. Res. Lett.*, vol. 25, no. 9, pp. 1335–1338, 1998.

[26] V. I. Khvorostyanov and K. Sassen, "Cirrus cloud simulation using explicit microphysics and radiation—Part II: Microphysics, vapor and ice mass budgets, and optical and radiative properties," *J. Atmos. Sci.*, vol. 55, pp. 1822–1833, 1998.

[27] J. P. Hollinger, J. L. Peirce, and G. A. Poe, "SSM/I instrument evaluation," *IEEE Trans. Geosci. Remote Sensing*, vol. 28, pp. 781–789, Sept. 1990.

[28] A. Stogryn, "The apparent temperature of the sea at microwave frequencies," *IEEE Trans. Antennas Propagat.*, vol. AP-15, pp. 278–286, 1967.

[29] T. Wilheit Jr., "A model for the microwave emissivity of the ocean's surface as a function of wind speed," *IEEE Trans. Geosci. Electron.*, vol. GE-17, pp. 244–249, 1979.

[30] P. W. Rosenkranz, "Rough-sea microwave emission measured with the SSM/I," *IEEE Trans. Geosci. Remote Sensing*, vol. 30, pp. 1081–1085, Sept. 1992.

[31] A. J. Gasiewski and D. B. Kunkee, "Polarized microwave emission from water waves," *Radio Sci.*, vol. 29, no. 6, pp. 1449–1466, 1994.

[32] J. R. Apel, "An improved model of the ocean surface wave vector spectrum and its effects on radar backscatter," *J. Geophys. Res.*, vol. 99, no. C8, pp. 16 269–16 291, 1994.

[33] J. Klinke and B. Jahne, "2D wave number spectra of short wind waves—Results from wind wave facility and extrapolation to the oceans," in *Optics of the Air-Sea Interface: Theory and Measurements, Proc. SPIE*, vol. 1749, 1992, pp. 1–13.

[34] B. Jahne and K. S. Riemer, "Two-dimensional wave number spectra of small-scale water surface waves," *J. Geophys. Res.*, vol. 95, pp. 11531–11 546, 1990.

[35] A. Guissard and P. Sobieski, "An approximate model for the microwave brightness temperature of the sea," *Int. J. Remote Sensing*, vol. 8, pp. 1607–1627, 1987.

[36] A. G. Voronovich, "Small-slope approximation in wave scattering by rough surfaces," *Sov. Phys. JETP*, vol. 62, no. 1, pp. 65–70, 1985.

LABORATORY OPERATIONS

The Aerospace Corporation functions as an "architect-engineer" for national security programs, specializing in advanced military space systems. The Corporation's Laboratory Operations supports the effective and timely development and operation of national security systems through scientific research and the application of advanced technology. Vital to the success of the Corporation is the technical staff's wide-ranging expertise and its ability to stay abreast of new technological developments and program support issues associated with rapidly evolving space systems. Contributing capabilities are provided by these individual organizations:

Electronics and Photonics Laboratory: Microelectronics, VLSI reliability, failure analysis, solid-state device physics, compound semiconductors, radiation effects, infrared and CCD detector devices, data storage and display technologies; lasers and electro-optics, solid state laser design, micro-optics, optical communications, and fiber optic sensors; atomic frequency standards, applied laser spectroscopy, laser chemistry, atmospheric propagation and beam control, LIDAR/LADAR remote sensing; solar cell and array testing and evaluation, battery electrochemistry, battery testing and evaluation.

Space Materials Laboratory: Evaluation and characterizations of new materials and processing techniques: metals, alloys, ceramics, polymers, thin films, and composites; development of advanced deposition processes; nondestructive evaluation, component failure analysis and reliability; structural mechanics, fracture mechanics, and stress corrosion; analysis and evaluation of materials at cryogenic and elevated temperatures; launch vehicle fluid mechanics, heat transfer and flight dynamics; aerothermodynamics; chemical and electric propulsion; environmental chemistry; combustion processes; space environment effects on materials, hardening and vulnerability assessment; contamination, thermal and structural control; lubrication and surface phenomena.

Space Science Application Laboratory: Magnetospheric, auroral and cosmic ray physics, wave-particle interactions, magnetospheric plasma waves; atmospheric and ionospheric physics, density and composition of the upper atmosphere, remote sensing using atmospheric radiation; solar physics, infrared astronomy, infrared signature analysis; infrared surveillance, imaging, remote sensing, and hyperspectral imaging; effects of solar activity, magnetic storms and nuclear explosions on the Earth's atmosphere, ionosphere and magnetosphere; effects of electromagnetic and particulate radiations on space systems; space instrumentation, design fabrication and test; environmental chemistry, trace detection; atmospheric chemical reactions, atmospheric optics, light scattering, state-specific chemical reactions and radiative signatures of missile plumes.

Center for Microtechnology: Microelectromechanical systems (MEMS) for space applications; assessment of microtechnology space applications; laser micromachining; laser-surface physical and chemical interactions; micropropulsion; micro- and nanosatellite mission analysis; intelligent microinstruments for monitoring space and launch system environments.

Office of Spectral Applications: Multispectral and hyperspectral sensor development; data analysis and algorithm development; applications of multispectral and hyperspectral imagery to defense, civil space, commercial, and environmental missions.